

Longitudinal magnetoconductivity in chiral multifold semimetals exemplified by pseudospin-1 nodal points

Ipsita Mandal*

*Department of Physics, Shiv Nadar Institution of Eminence (SNIOE),
Gautam Buddha Nagar, Uttar Pradesh 201314, India*

We embark on computing the longitudinal magnetoconductivity within the semiclassical Boltzmann formalism, where an isotropic triple-point semimetal (TSM) is subjected to collinear electric (\mathbf{E}) and magnetic (\mathbf{B}) fields. Except for the Drude part, the B -dependence arises exclusively from topological properties like the Berry curvature and the orbital magnetic moment. We solve the Boltzmann equations exactly in the linear-response regime, applicable in the limit of weak/nonquantising magnetic fields. The novelty of our investigation lies in the consideration of the truly multifold character of the TSMs, where the so-called flat-band (flatness being merely an artifact of linear-order approximations) is made dispersive by incorporating the appropriate quadratic-in-momentum correction in the effective Hamiltonian. It necessitates the consideration of interband scatterings within the same node as well, providing a complex interplay of intraband, interband, intranode, and internode processes, offering an overwhelmingly rich set of possibilities. The exact results are compared with those obtained from a naive relaxation-time approximation.

CONTENTS

I. Introduction	1
II. Model	2
III. Conductivity	3
A. Relevant topological quantities	3
B. Collinear electric and magnetic fields along the z -axis	4
C. Results and discussions	7
IV. Comparison with results obtained from relaxation-time approximation	8
A. Contribution from intranode parts	10
B. Contribution from internode parts	11
C. Overall characteristics	12
V. Summary, discussions, and future perspectives	12
Acknowledgments	12
Appendix: Matrix equation for determining the unknown coefficients	13
References	14

I. INTRODUCTION

Motivated by the ongoing interests in unravelling novel transport properties in three-dimensional (3d) nodal-point semimetals [1–8], we undertake the exercise of studying pseudospin-1 triple-point semimetals (TSMs) [5, 6, 8–16], with a quadratic correction renders the system more realistic [8, 17]. The 3d semimetals comprise an extremely broad and diverse family, with the degeneracy at the nodal point given by $(2\varsigma + 1)$, where the effective Hamiltonian in the vicinity of a node takes the form of $\mathbf{d}(\mathbf{k}) \cdot \mathbf{S}$, with $\mathbf{d}(\mathbf{k}) = \{d_x(\mathbf{k}), d_y(\mathbf{k}), d_z(\mathbf{k})\}$. The symbol \mathbf{S} stands for the vector operator comprising the components $\{S_x, S_y, S_z\}$, representing the three components of the angular-momentum operator in the spin- ς representation of the SU(2) group. Consequently, the $(2\varsigma + 1)$ -band system is said to carry the quantum numbers of pseudospin- ς , with the bands labelled by the S_z -projections spanning from $-\varsigma$ to ς . The minimal case of twofold degeneracy is represented by the pseudospin-1/2-valued Weyl semimetals (WSMs) [1–3], which is isotropic in the simplest scenarios. Its multifold cousins are captured by the pseudospin-1 TSMs and the pseudospin-3/2 Rarita-Schwinger-Weyl

* ipsita.mandal@snu.edu.in

(RSW) semimetal [5, 6, 8, 9, 12–14, 18–27], for example. All these systems exemplify bandstructures featuring nontrivial topology [28–30] induced by the Berry phases, which show up in the form of topological quantities like the Berry curvature (BC) and the orbital magnetic moment (OMM). These, in turn, source nontrivial features in the response, that can be measured in transport-experiments [4, 8, 26, 27, 31–35]. While our primary focus in this paper is computing longitudinal magnetotransport for TSMs with $\varsigma = 1$, other examples include intrinsic anomalous-Hall effects [36–38], planar-Hall coefficients [4, 8, 16, 26, 27, 31–35, 39–56], Magnus-Hall effect [23, 57, 58] circular dichroism [12, 59], and circular photogalvanic effect [60–63], to name a few. The effective low-energy model of a TSM comprises threefold-degenerate band-crossing points, as shown in Fig. 1, for which \mathbf{S} is written down in a spin-1 representation. The pseudospin-1 quasiparticles can be realised in widely-available systems and have been the focus of numerous studies [9, 11, 12, 15, 16, 48, 64–77]. In the literature, they have sometimes been referred to as “Maxwell fermions” [66], borrowing the terminology from the spin-1 quantum numbers of the photons, which emerge from the Maxwell equations for electromagnetism.

A nonzero BC-profile is accompanied by nonzero BC monopoles at the nodal points [78, 79], serving as topological charges, and sourcing the BC flux. These can be interpreted as Chern numbers, when we consider the topological properties of the 3d Brillouin zone (BZ) treated as a closed manifold. The sign of a Chern number is referred to as the chirality (χ) of the node, endowing a label of *handedness or chirality* to the quasiparticles associated with it. They are called *right-handed* or *left-handed* according to whether $\chi = 1$ or $\chi = -1$. Of course, a summation of all the Chern numbers over all the nodes in the BZ, carried either by the conduction or the valence bands, must yield zero for a system originating in a lattice. The mathematical proof of this phenomenon is provided by the Nielsen-Ninomiya theorem [80]. The outcome of this fact is that there exist conjugate pairs of nodes in the BZ, carrying $\chi = \pm 1$. Here, we will adhere to the convention of assigning χ the sign of the Chern numbers of the negative-energy bands, where positive or negative is measured with respect to the band-touching point (taken to set the zero of energy).

For topological semimetals, there exist extensive amounts of theoretical and experimental studies, trying to identify and characterise unique response coefficients [4, 8, 31–35, 39–43, 45–51, 53, 81, 82], which can reflect the underlying topology of the BZ. Nevertheless, more remains to be explored. For example, in our earlier works, we have computed the weak-magnetic-field-induced response in planar-Hall set-ups, in the limit of relaxation-time approximation. Here, we aim to perform an exact calculation of the longitudinal conductivity, arising from applying collinear electric (\mathbf{E}) and magnetic (\mathbf{B}) fields, by going beyond the relaxation-time approximation. This exercise has been carried out for WSMs [31, 83, 84], which we will carry out for TSMs, whose unphysical representation of a flat-band is remedied by adding a spherically-symmetric quadratic-in-momentum correction [17]. Hence, the flat-band will be promoted to a quadratically-dispersive band, which will now contribute to the net conductivity (as expected in an actual experiment [8]). We would like to point out that, in Ref. [85], the behaviour of the longitudinal conductivity has been discussed for TSMs with a nondispersive band, where it does not contribute, since quadratic corrections are not taken into account.

The paper is organized as follows: In Sec. II, we describe the explicit form of the low-energy effective Hamiltonian in the vicinity of a TSM node, after adding the appropriate quadratic correction. Sec. III is devoted to deriving the equations leading to the final values of the longitudinal magnetoconductivity. The results are discussed in Sec. III C therein, illustrated by representative plots. For examining the validity of the relaxation-time approximation for this multifold system, in Sec. IV, we rederive the conductivity using this simplifying assumption and compare it with the results obtained from the exact expressions. Finally, we conclude with a summary and outlook in Sec. V. In all our expressions, we will be using the natural units, which means that the reduced Planck’s constant (\hbar), the speed of light (c), and the Boltzmann constant (k_B) are each set to unity. Additionally, the electric charge has no units, with the magnitude of a single electronic charge measuring $e = 1$. Although e is equal to one, we will retain it in our expressions just as a matter of book-keeping.

II. MODEL

Our focus is on TSMs, which exist in materials hosting a pair of conjugate nodes with Chern numbers ± 2 in the BZ [5, 6, 10]. In particular, we will focus on isotropic nodes, obtained by expanding the $\mathbf{k} \cdot \mathbf{p}$ Hamiltonian about the threefold-degenerate points, in small $\{k_x, k_y, k_z\}$, valid in the low-energy limit. We note that, if we decide to expand upto linear-in-momentum, we get a flat band, which is of course an artifact of linear-order approximation and corresponds to an unphysical situation. Therefore, we retain the rotationally-symmetric terms upto quadratic-in-momentum, which is captured by the following effective continuum Hamiltonian [17]:

$$\mathcal{H}_\chi(\mathbf{k}) = \mathbf{d}(\mathbf{k}) \cdot \mathbf{S} + c v_F k^2 \mathbb{I}_{3 \times 3}, \quad \mathbf{d}(\mathbf{k}) = v_F \{k_x, k_y, \chi k_z\}, \quad k = \sqrt{k_x^2 + k_y^2 + k_z^2}. \quad (1)$$

Here, $\mathbf{S} = \{S_x, S_y, S_z\}$ represents the vector comprising the three components of the angular-momentum operator in the spin-1 representation of the $SO(3)$ group, $\chi \in \{1, -1\}$ denotes the chirality of the node, and v_F is the isotropic Fermi velocity. For our calculations, we have chosen the particular representation where

$$S_x = \frac{1}{\sqrt{2}} \begin{pmatrix} 0 & 1 & 0 \\ 1 & 0 & 1 \\ 0 & 1 & 0 \end{pmatrix}, \quad S_y = \frac{1}{\sqrt{2}} \begin{pmatrix} 0 & -i & 0 \\ i & 0 & -i \\ 0 & i & 0 \end{pmatrix}, \quad S_z = \begin{pmatrix} 1 & 0 & 0 \\ 0 & 0 & 0 \\ 0 & 0 & -1 \end{pmatrix}. \quad (2)$$

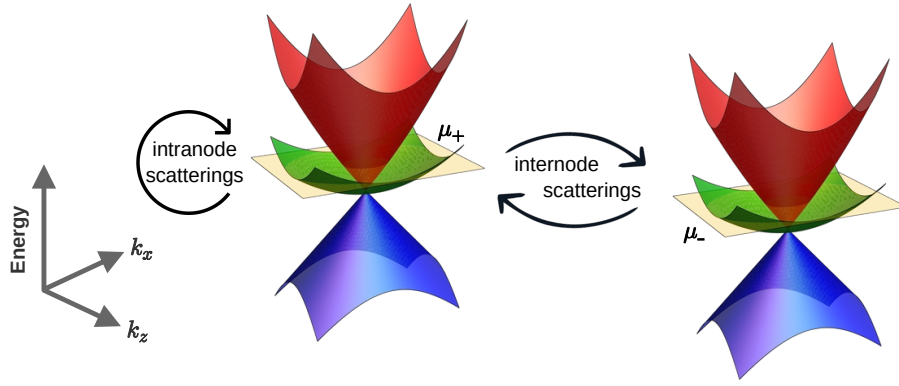


FIG. 1. Schematics of the scattering processes between two nodes of TSM of opposite values of chirality. The values of the chemical potential, represented by the yellow planes, have been tuned to cut the positive-energy bands at each node.

The energy eigenvalues of the Hamiltonian are given by

$$\varepsilon_s(\mathbf{k}) = s v_F k + c v_F k^2, \quad s \in \{-1, 0, 1\}, \quad (3)$$

as illustrated in Fig. 1. Setting c to zero makes the $s = 0$ band morph into a flat (i.e., nondispersive) band, as discussed above. We will consider the $c v_F k^2$ term to be the subdominant term for the $s = \pm 1$ bands, and choose $c > 0$ such that a positive chemical potential (μ) cuts the $s = 0$ band. The group-velocity of the chiral quasiparticles, occupying the band with index s , is given by

$$\mathbf{v}_s(\mathbf{k}) \equiv \nabla_{\mathbf{k}} \varepsilon_s(\mathbf{k}) = \frac{v_F (s + 2 c k)}{k} \{k_x, k_y, k_z\}. \quad (4)$$

Exploiting the spherical symmetry of the problem, we will work in the spherical polar coordinates, such that

$$k_x = k \sin \theta \cos \phi, \quad k_y = k \sin \theta \sin \phi, \quad k_z = k \cos \theta, \quad (5)$$

where $k \in [0, \infty)$, $\phi \in [0, 2\pi)$, and $\theta \in [0, \pi]$. For all the positive-energy bands, a set of normalised eigenvectors, $\{\psi_{\chi,s}(\mathbf{k})\}$, can be represented as follows:

$$\begin{aligned} & \begin{bmatrix} e^{-2i\phi} \cos^2(\frac{\theta}{2}) & \frac{e^{-i\phi} \sin \theta}{\sqrt{2}} & \sin^2(\frac{\theta}{2}) \end{bmatrix}^T & \text{for } \{\chi, s\} = \{1, 1\}, \\ & \begin{bmatrix} e^{-2i\phi} \sin^2(\frac{\theta}{2}) & -\frac{e^{-i\phi} \sin \theta}{\sqrt{2}} & \cos^2(\frac{\theta}{2}) \end{bmatrix}^T & \text{for } \{\chi, s\} = \{-1, 1\}, \\ & \begin{bmatrix} -\frac{e^{-2i\phi} \sin \theta}{\sqrt{2}} & e^{-i\phi} \cos \theta & \frac{\sin \theta}{\sqrt{2}} \end{bmatrix}^T & \text{for } \{\chi, s\} = \{\pm 1, 0\}. \end{aligned} \quad (6)$$

Here, we note that, since the $c v_F k^2$ correction accompanies the identity matrix, its addition does not alter the spinor structure of the eigenvectors, when compared to the models considered earlier (for example, in Refs. [6, 16]). Thus the topological properties like the BC and the OMM [see Eq. (7) below] also remain the same.

III. CONDUCTIVITY

In this section, we will outline the methodology to compute the conductivity using the semiclassical Boltzmann formalism [4, 26, 27, 29, 31, 86, 87].

A. Relevant topological quantities

We discuss here the vectors given by the Berry curvature (BC) and the orbital magnetic moment (OMM), which will affect the linear response that we are set out to compute. For the band with index s , these are expressed by the generic formulae of [28, 88]

$$\boldsymbol{\Omega}_{\chi,s}(\mathbf{k}) = i [\nabla_{\mathbf{k}} \psi_{\chi,s}(\mathbf{k})]^\dagger \times [\nabla_{\mathbf{k}} \psi_{\chi,s}(\mathbf{k})] \text{ and } \mathbf{m}_{\chi,s}(\mathbf{k}) = \frac{-ie}{2} [\nabla_{\mathbf{k}} \psi_{\chi,s}(\mathbf{k})]^\dagger \times \left[\{\mathcal{H}_{\chi}(\mathbf{k}) - \varepsilon_s(\mathbf{k})\} \nabla_{\mathbf{k}} \psi_{\chi,s}(\mathbf{k}) \right], \quad (7)$$

respectively. Here, $\{|\psi_{\chi,s}(\mathbf{k})\rangle\}$ is the set of normalized eigenvectors for the parent Hamiltonian. On evaluating the expressions in Eq. (7) using $\mathcal{H}_\chi(\mathbf{k})$, we get

$$\boldsymbol{\Omega}_{\chi,s}(\mathbf{k}) = \frac{-\chi s}{k^3} \{k_x, k_y, k_z\}, \quad \mathbf{m}_{\chi,s}(\mathbf{k}) = \frac{-\chi e v_F \mathcal{G}_s}{2 k^2} \{k_x, k_y, k_z\}, \quad \text{where } \mathcal{G}_s = \begin{cases} 1 & \text{for } s = \pm 1 \\ 2 & \text{for } s = 0 \end{cases}. \quad (8)$$

We note that, for the $s = 0$ band, although the BC is identically zero. However, the OMM is nonzero, turning out to be twice the OMM of the $s = \pm 1$ bands. Therefore, all the bands are endowed with nontrivial topological properties. It is easy to verify from the $\boldsymbol{\Omega}_{\chi,s}(\mathbf{k})$ -expressions that the node has a net Chern number of 2χ , contributed by the $s = \pm 1$ bands.

A nonzero BC modifies the phase-space volume element for the particles occupying a Bloch band, via the factor of $[\mathcal{D}_{\chi,s}(\mathbf{k})]^{-1}$, where

$$\mathcal{D}_{\chi,s}(\mathbf{k}) = [1 + e \{\mathbf{B} \cdot \boldsymbol{\Omega}_{\chi,s}(\mathbf{k})\}]^{-1}. \quad (9)$$

The presence of a nonzero OMM causes a Zeeman-like correction to the bare dispersion [28], leading to a net effective value of

$$\xi_{\chi,s}(\mathbf{k}) = \varepsilon_s(\mathbf{k}) + \varepsilon_{\chi,s}^{(m)}(\mathbf{k}), \quad \varepsilon_{\chi,s}^{(m)}(\mathbf{k}) = -\mathbf{B} \cdot \mathbf{m}_{\chi,s}(\mathbf{k}). \quad (10)$$

This, in turn, modifies the group-velocity as

$$\mathbf{w}_{\chi,s}(\mathbf{k}) \equiv \nabla_{\mathbf{k}} \xi_{\chi,s}(\mathbf{k}) = \mathbf{v}_s(\mathbf{k}) + \mathbf{v}_{\chi,s}^{(m)}(\mathbf{k}), \quad \mathbf{v}_{\chi,s}^{(m)}(\mathbf{k}) = \nabla_{\mathbf{k}} \varepsilon_{\chi,s}^{(m)}(\mathbf{k}). \quad (11)$$

The effects of OMM show up via the modified energy appearing in the equilibrium Fermi-Dirac distribution,

$$f_0(\xi_{\chi,s}(\mathbf{k}), \mu, T) = \frac{1}{1 + \exp[(\xi_{\chi,s}(\mathbf{k}) - \mu)/T]}, \quad (12)$$

where T is the temperature. While using f_0 in various equations, we will be suppressing its μ - and T -dependence for uncluttering of notations. Moreover, in what follows, we will restrict our calculations to the $T = 0$ limit.

In our earlier work, appearing as Ref. [16], we did not consider the quadratic corrections. Therefore, the flat-band there was ignored, considering the fact that a nonzero chemical potential (measured with respect to the nodal point) will not cut the band, leading to no contribution to conductivity. Of course the OMM would have given it a finite dispersion for a nonzero magnetic field — but it would lead to open Fermi surfaces, which would have necessitated the introduction of artificial cut-offs in the momentum-integrals. Such an unphysical situation is remedied by introducing the quadratic-in-momentum corrections.

B. Collinear electric and magnetic fields along the z -axis

Let us write down the expressions for the OMM-induced energy and velocity when $\mathbf{B} = B \hat{\mathbf{z}}$, aligned along an external electric field, $\mathbf{E} = E \hat{\mathbf{z}}$. For this case, we have

$$\varepsilon_{\chi,s}^{(m)}(\mathbf{k}) = \frac{\chi e B v_F \mathcal{G}_s k_z}{2 k^2} \quad \text{and} \quad \mathbf{u}_{\chi,s}^{(m)}(\mathbf{k}) = \frac{-\chi e B v_F \mathcal{G}_s}{k^4} \left\{ k_z k_x, k_y k_z, \frac{k_z^2 - k_x^2 - k_y^2}{2} \right\}. \quad (13)$$

The Hamilton's equations of motion for the chiral quasiparticles, subjected to collinear electric (\mathbf{E}) and magnetic (\mathbf{B}) fields, are given by [4, 26, 27, 29, 86, 87]

$$\begin{aligned} \dot{\mathbf{r}} &= \nabla_{\mathbf{k}} \xi_{\chi,s} - \dot{\mathbf{k}} \times \boldsymbol{\Omega}_{\chi,s}(\mathbf{k}) \quad \text{and} \quad \dot{\mathbf{k}} = -e(\mathbf{E} + \dot{\mathbf{r}} \times \mathbf{B}) \\ \Rightarrow \dot{\mathbf{r}} &= \mathcal{D}_{\chi,s}(\mathbf{k}) [\mathbf{w}_{\chi,s}(\mathbf{k}) + e \mathbf{E} \times \boldsymbol{\Omega}_{\chi,s}(\mathbf{k}) + e \{\boldsymbol{\Omega}_{\chi,s} \cdot \mathbf{w}_{\chi,s}(\mathbf{k})\} \mathbf{B}] \\ \text{and } \dot{\mathbf{k}} &= -e \mathcal{D}_{\chi,s}(\mathbf{k}) [\mathbf{E} + \mathbf{w}_{\chi,s}(\mathbf{k}) \times \mathbf{B} + e(\mathbf{E} \cdot \mathbf{B}) \boldsymbol{\Omega}_{\chi,s}(\mathbf{k})]. \end{aligned} \quad (14)$$

where $-e$ is the quantum of charge for each quasiparticle. We note that a nonzero BC has modified the form of the Hamilton's equations of motion compared to the cases when the BC is zero (see, for example, the systems discussed in Refs. [89, 90]). Clearly, the $-\dot{\mathbf{k}} \times \boldsymbol{\Omega}_{\chi,s}$ term in the expression for $\dot{\mathbf{r}}$ acts as an anomalous velocity, with the BC being an analogue of the magnetic field in the momentum space (comparing with the $-e \dot{\mathbf{r}} \times \mathbf{B}$ term appearing in the expression for $\dot{\mathbf{k}}$). The kinetic equation, arising out of the fundamental Boltzmann formalism to compute transport, is expressed as

$$[\partial_t + \mathbf{w}_{\chi,s}(\mathbf{k}) \cdot \nabla_{\mathbf{r}} - e \{\mathbf{E} + \mathbf{w}_{\chi,s}(\mathbf{k}) \times \mathbf{B}\} \cdot \nabla_{\mathbf{k}}] f_{\chi,s}(\mathbf{r}, \mathbf{k}, t) = I_{\text{coll}}[f_{\chi,s}(\mathbf{k})], \quad (15)$$

where $f_{\chi,s}(\mathbf{r}, \mathbf{k}, t)$ represents the nonequilibrium quasiparticle-distribution function close to the semimetallic node of chirality χ . The deviation, $\delta f_{\chi,s}(\mathbf{r}, \mathbf{k}, t) \equiv f_{\chi,s}(\mathbf{r}, \mathbf{k}, t) - f_0(\xi_{\chi,s}(\mathbf{k}))$, from the equilibrium distribution, $f_0(\xi_{\chi,s}(\mathbf{k}))$, is caused by the probe field, \mathbf{E} , coupled with the nonquantising \mathbf{B} -field, whose magnitude is controlled by the magnitude of \mathbf{E} (which itself is assumed to be small). Here, we restrict ourselves to time-independent and spatially-uniform external fields and, hence, $f_{\chi,s}$ must not depend on position and time, implying $\delta f_{\chi,s}(\mathbf{r}, \mathbf{k}, t) = \delta f_{\chi,s}(\mathbf{k})$. Expanding upto order $|\mathbf{E}|$ in smallness allows us to arrive at the linearised approximation for the resulting response coefficients. On the right-hand side, $I_{\text{coll}}[f_{\chi,s}(\mathbf{k})]$ symbolises the so-called *collision integral*, which comprises the relevant scattering processes trying to relax $f_{\chi,s}(\mathbf{k})$ towards $f_0(\xi_{\chi,s}(\mathbf{k}))$.

For point-scattering mechanisms, the collision integral takes the form of

$$I_{\text{coll}}[f_{\chi,s}(\mathbf{k})] = \sum_{\tilde{\chi}, \tilde{s}} \int_{\mathbf{k}'} \mathcal{M}_{s,\tilde{s}}^{\chi,\tilde{\chi}}(\mathbf{k}, \mathbf{k}') [f_{\tilde{\chi},\tilde{s}}(\mathbf{k}') - f_{\chi,s}(\mathbf{k})], \quad (16)$$

where $\int_{\mathbf{k}} \equiv \int d^3\mathbf{k} D_{\tilde{\chi},\tilde{s}}^{-1}(\mathbf{k}')/(2\pi)^3$ denotes the three-dimensional integral in the momentum space, containing the modified phase-space factor due to the BC. The scattering rate, parametrised by

$$\mathcal{M}_{s,\tilde{s}}^{\chi,\tilde{\chi}}(\mathbf{k}, \mathbf{k}') = \frac{2\pi\rho_{\text{imp}}}{V} \left| \{\psi_{\tilde{\chi},\tilde{s}}(\mathbf{k}')\}^\dagger \mathcal{V}_{s,\tilde{s}}^{\chi,\tilde{\chi}}(\mathbf{k}, \mathbf{k}') \psi_{\chi,s}(\mathbf{k}) \right|^2 \delta(\xi_{\tilde{\chi},\tilde{s}}(\mathbf{k}') - \xi_{\chi,s}(\mathbf{k})), \quad (17)$$

is obtained by applying the Fermi's golden rule, where ρ_{imp} represents the impurity-concentration (acting as the scattering centres), V denotes the system's volume, and $\mathcal{V}_{s,\tilde{s}}^{\chi,\tilde{\chi}}(\mathbf{k}, \mathbf{k}')$ stands for the scattering-potential matrix (in the spinor space of the three-component wavevectors) convoluted to the momentum space. Here, we focus on elastic and nonmagnetic scatterings, for which $\mathcal{V}_{s,\tilde{s}}^{\chi,\tilde{\chi}}(\mathbf{k}, \mathbf{k}') = \mathbb{I}_{3 \times 3} \mathcal{V}_{s,\tilde{s}}^{\chi,\tilde{\chi}}$, which reduces to an identity matrix in the spinor space and does not have any momentum dependence. Therefore, the scattering rate simplifies to

$$\mathcal{M}_{s,\tilde{s}}^{\chi,\tilde{\chi}}(\mathbf{k}, \mathbf{k}') = \frac{2\pi\rho_{\text{imp}} |\mathcal{V}_{s,\tilde{s}}^{\chi,\tilde{\chi}}|^2}{V} \left| \{\psi_{\tilde{\chi},\tilde{s}}(\mathbf{k}')\}^\dagger \psi_{\chi,s}(\mathbf{k}) \right|^2 \delta(\xi_{\tilde{\chi},\tilde{s}}(\mathbf{k}') - \xi_{\chi,s}(\mathbf{k})). \quad (18)$$

Assuming an interchange-symmetry between the $\chi = \pm 1$ nodes and the values of the bands, we enlist the associated scattering strengths as

$$|\mathcal{V}_{s,\tilde{s}}^{1,-1}|^2 = |\mathcal{V}_{s,\tilde{s}}^{-1,1}|^2 \equiv \frac{4\pi}{\rho_{\text{imp}}} \beta_{s,\tilde{s}}^{\text{inter}}, \quad |\mathcal{V}_{s,\tilde{s}}^{1,1}|^2 = |\mathcal{V}_{s,\tilde{s}}^{-1,-1}|^2 \equiv \frac{4\pi}{\rho_{\text{imp}}} \beta_{s,\tilde{s}}^{\text{intra}}, \quad \beta_{1,0}^{\text{inter}} = \beta_{0,1}^{\text{inter}}, \quad \beta_{1,0}^{\text{intra}} = \beta_{0,1}^{\text{intra}}. \quad (19)$$

Here, we need to solve the *linearised Boltzmann equation*, captured by

$$-e \mathcal{D}_{\chi,s}(\mathbf{k}) \left[\left\{ \mathbf{w}_{\chi,s}(\mathbf{k}) + e \left(\boldsymbol{\Omega}_{\chi,s}(\mathbf{k}) \cdot \mathbf{w}_{\chi,s}(\mathbf{k}) \right) \mathbf{B} \right\} \cdot \mathbf{E} \frac{\partial f_0(\xi_{\chi,s}(\mathbf{k}))}{\partial \xi_{\chi,s}(\mathbf{k})} + \{ \mathbf{w}_{\chi,s}(\mathbf{k}) \times \mathbf{B} \} \cdot \nabla_{\mathbf{k}} \delta f_{\chi,s}(\mathbf{k}) \right] = I_{\text{coll}}[f_{\chi,s}(\mathbf{k})]. \quad (20)$$

To solve the above equation, we parametrise the deviation as

$$\delta f_{\chi,s}(\mathbf{k}) = -e \frac{\partial f_0(\xi_{\chi,s})}{\partial \xi_{\chi,s}} \mathbf{E} \cdot \boldsymbol{\Lambda}_{\chi,s}(\mathbf{k}) = -e \frac{\partial f_0(\xi_{\chi,s}(\mathbf{k}))}{\partial \xi_{\chi,s}(\mathbf{k})} E \Lambda_{\chi,s}^z(\mathbf{k}), \quad (21)$$

where $\boldsymbol{\Lambda}_{\chi,s}(\mathbf{k})$ is the vectorial mean-free path. For our configuration, we get a nontrivial equation only for the z -component of $\boldsymbol{\Lambda}_{\chi,s}(\mathbf{k})$ as follows:

$$w_{\chi,s}^z(\mathbf{k}) + eB [\boldsymbol{\Omega}_s^x(\mathbf{k}) \cdot \mathbf{w}_{\chi,s}(\mathbf{k})] - eB [\mathbf{w}_{\chi,s}(\mathbf{k}) \times \hat{\mathbf{z}}(\mathbf{k})] \cdot \nabla_{\mathbf{k}} \Lambda_{\chi,s}^z(\mathbf{k}) = \mathcal{D}_{\chi,s}^{-1}(\mathbf{k}) \sum_{\tilde{\chi}, \tilde{s}} \int_{\mathbf{k}'} \mathcal{M}_{s,\tilde{s}}^{\chi,\tilde{\chi}}(\mathbf{k}, \mathbf{k}') [\Lambda_{\tilde{\chi},\tilde{s}}^z(\mathbf{k}') - \Lambda_{\chi,s}^z(\mathbf{k})]. \quad (22)$$

To solve the above equation, we take the self-consistent ansatz [31] that $\Lambda_{\chi,s}^z \equiv \Lambda_{\chi,s}^z(\mu, \theta)$ at an energy μ , which only depends on the polar angle, θ , and the chemical potential, μ . This is because, for elastic scattering, the integral over the full momentum space can be replaced by an integral over the Fermi surface at energy $\xi_{\chi,s}(\mathbf{k}) = \mu$, and the dependence on the azimuthal angle ϕ should not be there because of the rotational symmetry of the entire system in the $k_x k_y$ -plane. Consequently, the momentum-space integrals reduce to the respective Fermi surfaces at energy $\xi_{\chi,s}(k_F^{\chi,s}, \theta) = \mu$ with T set to zero, denoted by the set of Fermi momenta, $\{k_F^{\chi,s}(\theta)\}$. The self-consistency can be easily checked from the fact that $[\boldsymbol{\Omega}_s^x(\mathbf{k}) \cdot \mathbf{w}_{\chi,s}(\mathbf{k})]$ is ϕ -independent and $[\mathbf{w}_{\chi,s}(\mathbf{k}) \times \hat{\mathbf{z}}] \cdot \nabla_{\mathbf{k}} \Lambda_{\chi,s}^z(\mu, \theta)$ evaluates to zero.

Going by the above understanding, for our exercise involving $\mathbf{E} \parallel \mathbf{B}$, although the spinor overlaps contain the azimuthal angles, ϕ and ϕ' , they will drop out on performing the azimuthal-angle integrations. Hence, using Eq. (6), we can effectively

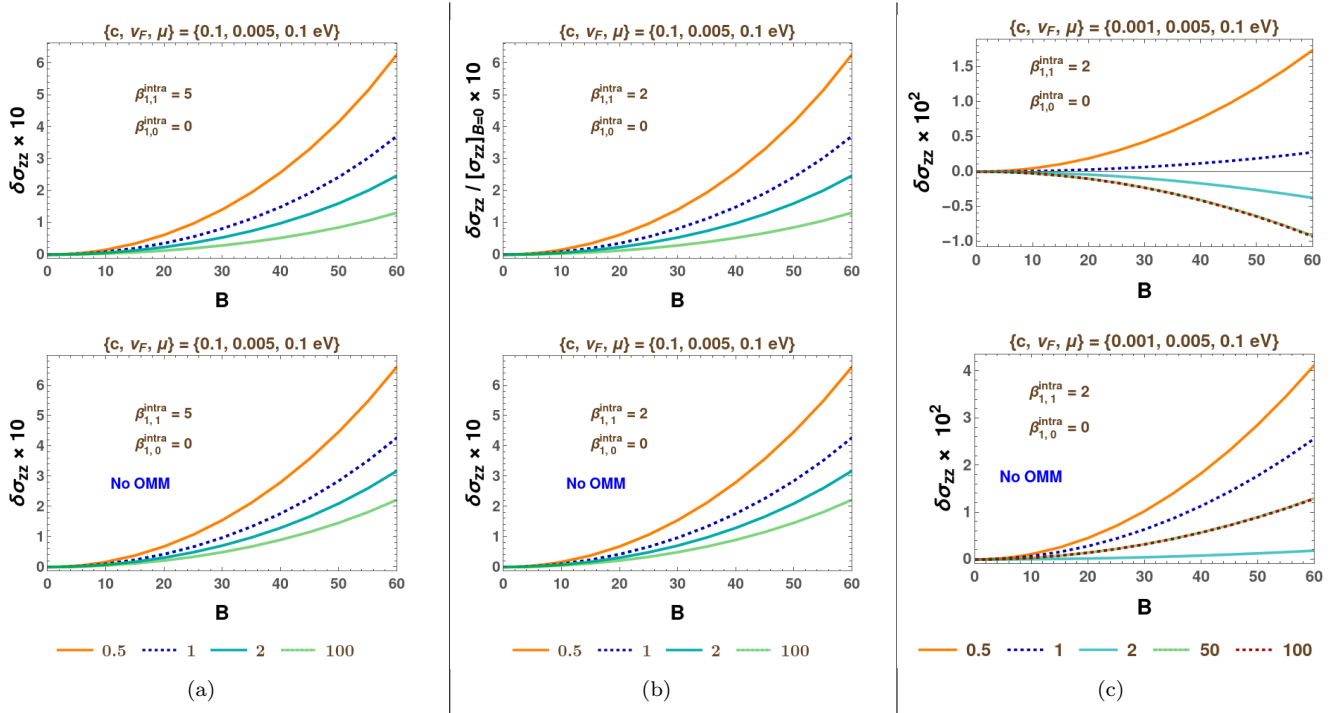


FIG. 2. $\delta\sigma_{zz}$ from the $\{s, \tilde{s}\} = \{1, 1\}$ bands with no interaction with the $\{s, \tilde{s}\} = \{0, 0\}$ bands: While the top panel shows the variation of the full conductivity with B (in eV^2) when OMM is taken into account appropriately, the bottom panel represents the conductivity versus B when OMM is not considered. The plot-legends indicate the values of the ratio $\beta_{1,1}^{\text{inter}}/\beta_{1,1}^{\text{intra}}$. The three subfigures represent three distinct sets of parameter values, as indicated in the labels.

use the overlap-function defined as

$$\begin{aligned}
 \mathcal{T}_{s,\tilde{s}}^{\chi,\tilde{\chi}}(\theta, \theta') = & \left[\sin^4\left(\frac{\theta}{2}\right) \sin^4\left(\frac{\theta'}{2}\right) + \frac{1}{4} \sin^2\theta \sin^2\theta' + \cos^4\left(\frac{\theta}{2}\right) \cos^4\left(\frac{\theta'}{2}\right) \right] \delta_{s,1} \delta_{\tilde{s},1} \\
 & + \left[\frac{\sin^2\theta \sin^2\theta'}{2} + \cos^2\theta \cos^2\theta' \right] \delta_{s,0} \delta_{\tilde{s},0} \\
 & + \left[\left\{ \sin^4\left(\frac{\theta}{2}\right) + \cos^4\left(\frac{\theta}{2}\right) \right\} \sin^2\theta' + \sin^2\theta \cos^2\theta' \right] \delta_{s,1} \delta_{\tilde{s},0} \\
 & + \left[\sin^2\theta \left\{ \sin^4\left(\frac{\theta'}{2}\right) + \cos^4\left(\frac{\theta'}{2}\right) \right\} + \cos^2\theta \sin^2\theta' \right] \delta_{s,0} \delta_{\tilde{s},1},
 \end{aligned} \tag{23}$$

while evaluating the integrals. Using the ϕ -independent forms, Eq. (22) reduces to

$$h_{\chi,s}(\mu, \theta) = \sum_{\tilde{\chi}, \tilde{s}} V \int_{k'} \mathcal{M}_{s,\tilde{s}}^{\chi,\tilde{\chi}}(\mathbf{k}, \mathbf{k}') \Lambda_{\tilde{\chi}, \tilde{s}}^z(\mu, \theta') - \frac{\Lambda_{\chi,s}^z(\mu, \theta)}{\tau_{\chi,s}(\mu, \theta)}, \tag{24}$$

where

$$\tau_{\chi,s}^{-1}(\mu, \theta) = \sum_{\tilde{\chi}, \tilde{s}} V \int_{k'} \mathcal{M}_{s,\tilde{s}}^{\chi,\tilde{\chi}}(\mathbf{k}, \mathbf{k}'), \quad h_{\chi,s}(\mu, \theta) = \mathcal{D}_{\chi,s}(\mathbf{k}) [w_{\chi,s}^z(\mathbf{k}) + eB \{\boldsymbol{\Omega}_s^{\chi}(\mathbf{k}) \cdot \mathbf{w}_{\chi,s}(\mathbf{k})\}]. \tag{25}$$

Since the integrals reduce to the respective Fermi surfaces at energy μ with T set to zero, the above expression further simplifies to

$$h_{\chi,s}(\mu, \theta) + \frac{\Lambda_{\chi,s}^z(\mu, \theta)}{\tau_{\chi,s}(\mu, \theta)} = \sum_{\tilde{\chi}, \tilde{s}} \frac{\rho_{\text{imp}} |\mathcal{V}_{s,\tilde{s}}^{\chi,\tilde{\chi}}|^2}{4\pi} \int d\theta' \frac{\sin\theta' (k')^3 \mathcal{D}_{\tilde{\chi}, \tilde{s}}^{-1}(\mathbf{k}')}{|\mathbf{k}' \cdot \mathbf{w}_{\chi,s}(\mathbf{k}')|} \mathcal{T}_{s,\tilde{s}}^{\chi,\tilde{\chi}}(\theta, \theta') \Lambda_{\tilde{\chi}, \tilde{s}}^z(\mu, \theta') \Big|_{k'=k_F^{\tilde{\chi}, \tilde{s}}}. \tag{26}$$

While the factor $(k')^3 \sin\theta'$ arises as the Jacobian for switching to the spherical polar coordinates, the part

$$|\hat{\mathbf{k}}' \cdot \nabla_{\mathbf{k}'} \xi_{\chi,s}(\mathbf{k}')|^{-1} = k' / |\mathbf{k}' \cdot \mathbf{w}_{\chi,s}(\mathbf{k}')|$$

arises from converting $\delta(\xi_{\tilde{\chi},\tilde{s}}(\mathbf{k}') - \mu)$ to $\delta(k' - k_F^{\tilde{\chi},\tilde{s}})$.

Noting the form of the wavevectors and their overlaps [cf. Eqs. (22) and (23)], we now make the following ansatz:

$$\begin{aligned}\Lambda_{\chi,1}^z(\mu, \theta) &= \tau_{\chi,1}(\mu, \theta) \left[-h_{\chi,1}(\mu, \theta) + a_{\chi,1} \cos^4\left(\frac{\theta}{2}\right) + b_{\chi,1} \cos^4\left(\frac{\theta}{2}\right) + c_{\chi,1} \sin^2\theta \right], \\ \Lambda_{\chi,0}^z(\mu, \theta) &= \tau_{\chi,0}(\mu, \theta) \left[-h_{\chi,0}(\mu, \theta) + c_{\chi,0} \sin^2\theta + d_{\chi,0} \cos^2\theta \right],\end{aligned}\quad (27)$$

corresponding to the two positive-energy bands at each node. This leaves us with the problem of solving for the 10 unknown coefficients, $\{a_{\chi,1}, b_{\chi,1}, c_{\chi,1}, c_{\chi,0}, d_{\chi,0}\}$, which must be real numbers. Plugging in the ansatz in Eq. (26) furnishes ten linear equations, which can be written as a matrix equation of the form

$$\mathcal{A}\mathcal{C} = \mathcal{H}, \text{ where } \mathcal{C} = [a_{1,1} \ b_{1,1} \ c_{1,1} \ c_{1,0} \ d_{1,0} \ a_{-1,1} \ b_{-1,1} \ c_{-1,1} \ c_{-1,0} \ d_{-1,0}]^T. \quad (28)$$

Additionally, the electron-number conservation furnishes the constraint of

$$\sum_{\chi,s} \int_{\mathbf{k}} \delta f_{\chi,s}(\mathbf{k}) = 0. \quad (29)$$

The explicit forms of the matrices are shown in the appendix.

Inserting the solutions, we obtain the charge-current density along the z -direction as

$$J_z^{\text{tot}} = -\frac{e}{V} \sum_{\chi,s} \int_{\mathbf{k}} (\dot{\mathbf{r}} \cdot \hat{\mathbf{z}}) \delta f_{\chi,s}(\mathbf{k}), \quad (30)$$

leading to

$$\sigma_{zz}^{\text{tot}} = -\frac{e^2}{V} \sum_{\chi,s} \int \frac{d^3\mathbf{k}}{(2\pi)^3} [w_{\chi,s}^z(\mathbf{k}) + eB \{\boldsymbol{\Omega}_{\chi,s}(\mathbf{k}) \cdot \mathbf{w}_{\chi,s}(\mathbf{k})\}] \delta(\xi_{\chi,s}(\mathbf{k}) - \mu) \Lambda_{\chi,s}^z(\mu, \theta). \quad (31)$$

C. Results and discussions

We now discuss the numerical results obtained by solving Eq. (26). For each case, we demonstrate the behaviour of

$$\delta\sigma_{zz} \equiv \sigma_{zz}(B)/\sigma_{zz}(B=0) - 1$$

for some representative parameter values, which will help visualising the interplay between the values of c and $\{\beta_{s,\tilde{s}}^{\text{intra}}, \beta_{s,\tilde{s}}^{\text{inter}}\}$. Depending on the context, $\sigma_{zz}(B)$ will represent the contribution from one particular type of band (i.e., with a particular value of S_z quantum number) from one individual node or both the nodes. For each of s and \tilde{s} taking the value of zero, the entire B -dependent conductivity is caused by the OMM, because the BC is zero for these bands. However, for the linear bands with small quadratic corrections, both the BC and the OMM contribute. Therefore, for these bands, in order to determine what the error would amount to if the OMM is not considered, we provide comparison-curves representing the cases when OMM is omitted. For all our plots, we have set $v_F = 0.005$ and $\mu = 0.1$ eV.

First, let us consider the case when the scattering processes obey the conditions $\beta_{s,\tilde{s}}^{\text{intra}} \propto \delta_{s,\tilde{s}}$ and $\beta_{s,\tilde{s}}^{\text{inter}} \propto \delta_{s,\tilde{s}}$, i.e., the quasiparticles carrying pseudospin-projection values of 1 and 0 do not talk to each other. Consequently, \mathcal{A} decomposes into the direct sum of the two matrices, \mathcal{A}_1 and \mathcal{A}_0 , where the former (latter) is a 6-dimensional (4-dimensional) square matrix. In every case, we find that \mathcal{A}_1 has rank 5 (instead of 6) and, hence, needs to be supplemented by the conservation equation, $\sum_{\chi} \int_{\mathbf{k}} \delta f_{\chi,1}(\mathbf{k}) = 0$, to determine all the unknown coefficients. Similarly, \mathcal{A}_0 has rank 3 (instead of 4) and the conservation equation, $\sum_{\chi} \int_{\mathbf{k}} \delta f_{\chi,0}(\mathbf{k}) = 0$, must be used to determine all the unknown coefficients. Figs. 2 and 3 capture such a scenario for the bands 1 and 0, respectively, each curve showing a $\propto B^2$ -dependence at leading order. For the linear bands with small quadratic corrections, in each case, the BC-only and OMM-induced parts have opposite signs. In fact, when $\beta_{1,1}^{\text{inter}}/\beta_{1,1}^{\text{intra}} > 1$ and is bigger than a threshold, the OMM acquires a large magnitude, thus managing to flip the sign of $\delta\sigma_{zz}$, which also crucially depends on the values of c [cf. Fig. 2 (c)]. For the $s = \tilde{s} = 0$ bands, sourced only by the OMM, $\delta\sigma_{zz}$ (representing the sum over both the nodes) is always negative. We also look into the behaviour a bit deeper by disentangling the contributions for the $\chi = +1$ and $\chi = -1$ nodes separately, originating from the $s = \tilde{s} = 0$ bands. In general, we find that they are asymmetric/unequal for a nonzero B , with the magnitude of $\delta\sigma_{zz}|_{\chi=-1}$ dominating over that of $\delta\sigma_{zz}|_{\chi=+1}$. While $\delta\sigma_{zz}|_{\chi=-1}$ always remain negative, for optimally low values of the internode-scattering amplitude, we find that $\delta\sigma_{zz}|_{\chi=+1}$ is positive. The latter behaviour can be nicely fitted with a curve of the form $aB^2 - bB^4$, where $a > 0$ and $b > 0$. However, the total, $\sum_{\chi} \delta\sigma_{zz}|_{\chi}$ is always negative, as reported above.

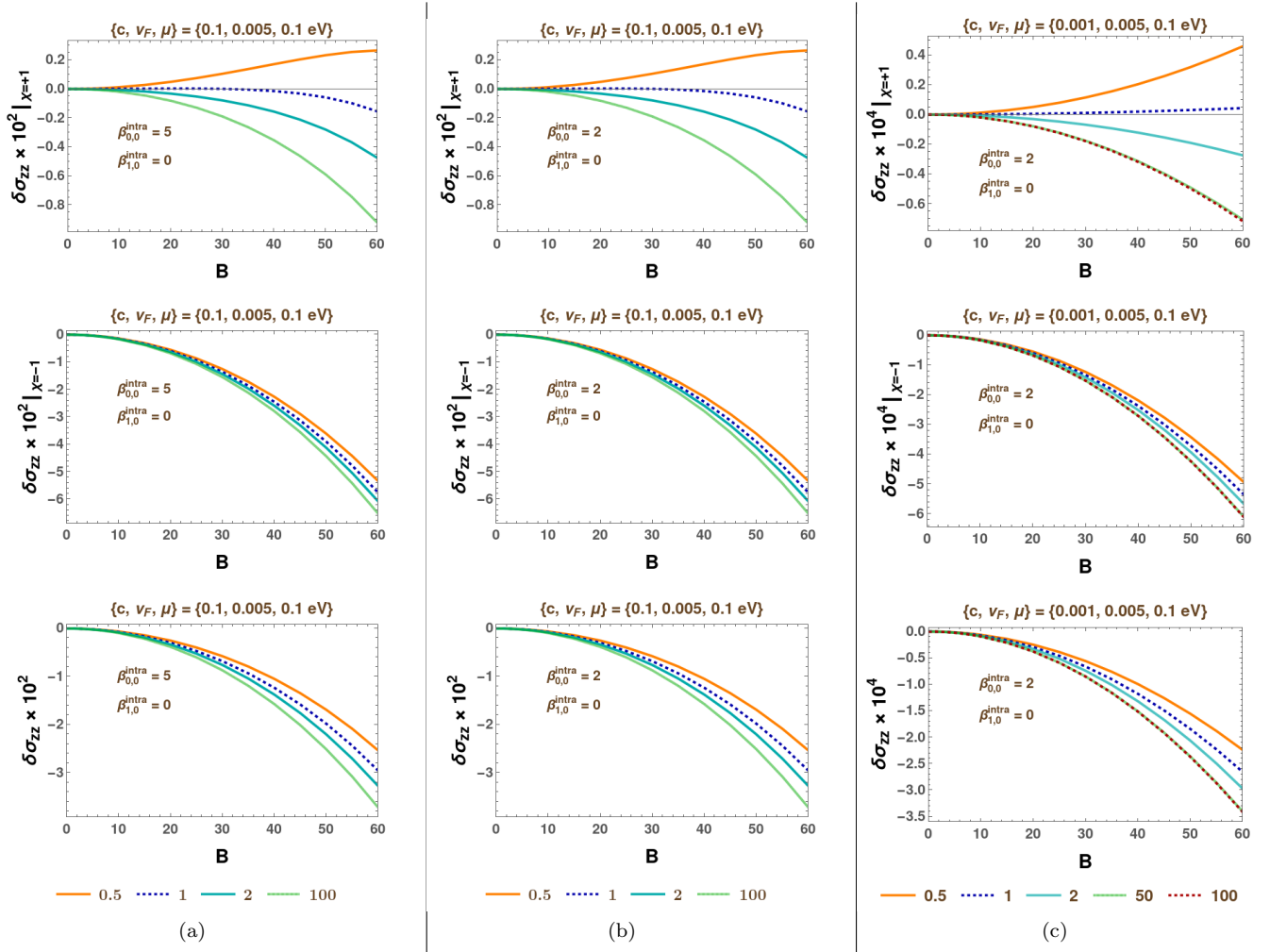


FIG. 3. $\delta\sigma_{zz}$ from the $\{s, \tilde{s}\} = \{0, 0\}$ bands with no interaction with the $\{s, \tilde{s}\} = \{1, 1\}$ bands: The curves demonstrate the variation of conductivity with B (in eV^2). Here, the B -dependence is entirely caused by the OMM, since BC is zero for these bands. The top, middle, and bottom panels represent the results for the $\chi = +1$ node, $\chi = -1$ node, and sum over both the nodes, respectively. The plot-legends indicate the values of the ratio $\beta_{0,0}^{\text{inter}}/\beta_{0,0}^{\text{intra}}$. The three subfigures represent three distinct sets of parameter values, as indicated in the labels.

Next, we consider the case when quasiparticles of all the participating conduction bands can scatter with one another. Figs. 4, 5, and 6 are the illustrations representative for this scenario. In particular, Fig. 6 captures the behaviour for a low ratio of c/v_F , corresponding to the parameters used in Figs. 2(c) and Figs. 3(c). On explicit computation, the 10-dimensional square matrix \mathcal{A} is found to have rank 9. Therefore, Eq. (29) must be used to determine all the unknown coefficients. Here too we find that, for the linear bands with small quadratic corrections, the OMM-contribution has a sign opposite to that of the BC-only-induced parts. For the $s = \tilde{s} = 0$ bands. For the $s = \tilde{s} = 0$ bands, the asymmetric χ -dependent characteristics persist, such that $\delta\sigma_{zz}|_{\chi=-1}$ always remain negative and, for low-enough values of internode-scattering amplitude, we find that $\delta\sigma_{zz}|_{\chi=+1}$ has positive values. Furthermore, a high value $\beta_{1,0}^{\text{intra}}$ of pushes $\delta\sigma_{zz}|_{\chi=+1}$ towards positive values as well [cf. Fig. 5(c)]. the Summing over the two nodes yields an overall negative value of $\delta\sigma_{zz}$ for these bands. Hence, our trial datasets reveal an incredible amount of tunability in obtaining a desired nature of the conductivity.

IV. COMPARISON WITH RESULTS OBTAINED FROM RELAXATION-TIME APPROXIMATION

In this section, we employ the simplistic application of the relaxation-time approximation, which we have used in our earlier works [16, 26, 27, 32–35, 82]. In this approach, the intranode- and internode-scattering-related currents need to be computed separately, with the multifold nature of the nodal points to be accounted for while calculating the internodal parts [82]. In order to obtain closed-form analytical expressions, we have to expand the B -dependent terms upto a given order in B , assuming it has a small magnitude, which is anyway required to justify neglecting the formation of the Landau

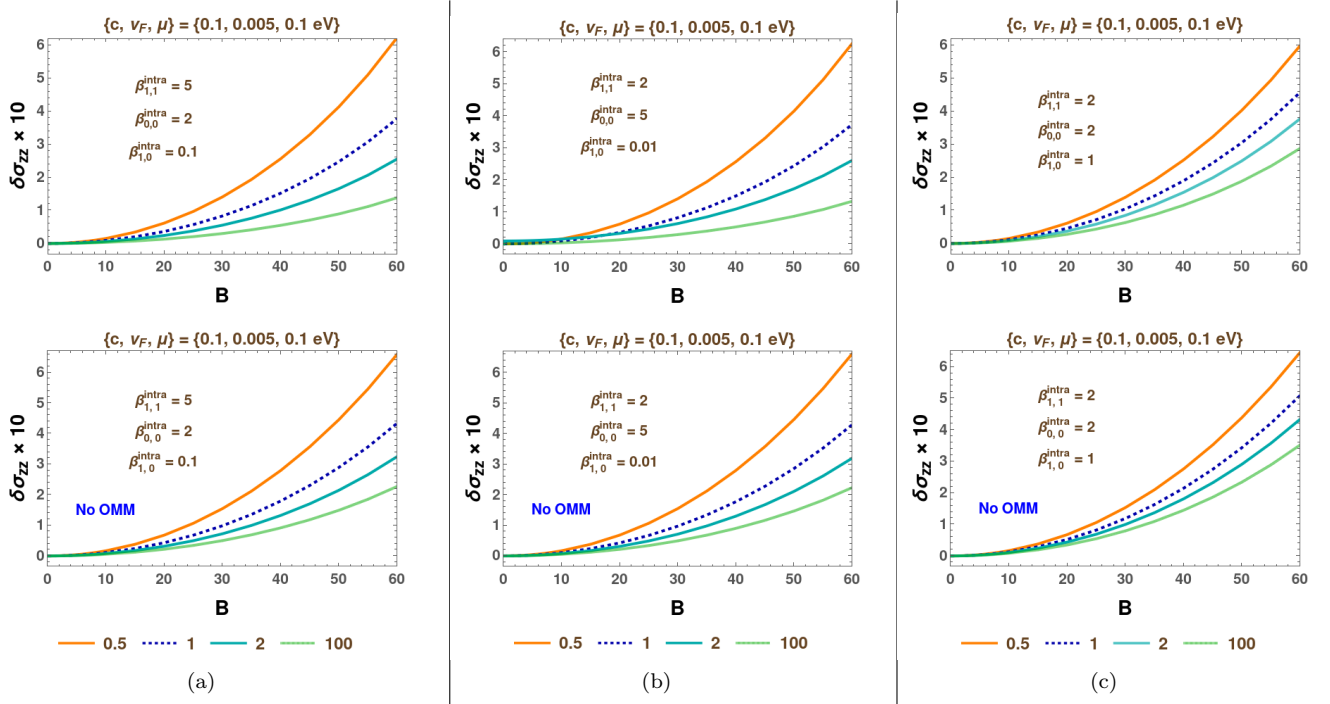


FIG. 4. $\delta\sigma_{zz}$ from the $\{s, \tilde{s}\} = \{1, 1\}$ bands interacting with the $\{s, \tilde{s}\} = \{0, 0\}$ bands: While the top panel shows the variation of the full conductivity of the $\{s, \tilde{s}\} = \{1, 1\}$ bands against B (in eV^2) when OMM is taken into account appropriately, the bottom panel represents the conductivity versus B when OMM is omitted. The plot-legends indicate the values of the ratios $\{\beta_{s,\tilde{s}}^{\text{inter}}/\beta_{s,\tilde{s}}^{\text{intra}}\}$. The three subfigures represent three distinct sets of parameter values, as indicated in the labels.

levels. With this in mind, the various quantities are expanded as follows:

$$f'_0(\xi_{\chi,s}) = f'_0(\varepsilon_{\chi,s}) + \varepsilon_{\chi,s}^{(m)} f''_0(\varepsilon_{\chi,s}) + \frac{1}{2} [\varepsilon_{\chi,s}^{(m)}]^2 f'''_0(\varepsilon_{\chi,s}) + \mathcal{O}(B^3), \quad (32)$$

and

$$\mathcal{D}_{\chi,s} = \sum_{n=0}^2 [-e\Omega_{\chi,s}^z B]^n + \mathcal{O}(B^3). \quad (33)$$

Here, the “prime” superscript denotes the operation of partial-differentiation, with respect to the variable shown explicitly within the brackets [e.g., $f'_0(\varepsilon) \equiv \partial_\varepsilon f_0(\varepsilon)$]. Since we are working in the $T \rightarrow 0$ limit, we have to use $f'_0(\varepsilon) \rightarrow -\delta(\varepsilon - \mu)$. Observing that the radial part of the integrals is with respect to the variable k , we need to use the following forms of the concerned expressions:

$$f''_0(\varepsilon_{\chi,s}(k)) = \frac{\partial_k f'_0(\varepsilon_{\chi,s}(k))}{2ckv_F + sv_F}, \quad f'''_0(\varepsilon_{\chi,s}(k)) = \frac{\partial_k^2 f'_0(\varepsilon_{\chi,s}(k))}{v_F^2(2ck + s)^2} - \frac{2c\partial_k f'_0(\varepsilon_{\chi,s}(k))}{v_F^2(2ck + s)^3}. \quad (34)$$

For the intranode parts, the analytical expressions are evaluated using the mother formula of [16, 26]

$$\sigma_{ij}^{\text{intra}}(\chi, s) = -e^2 \tau \int \frac{d^3 \mathbf{k}}{(2\pi)^3} \mathcal{D}_{\chi,s} [(w_{\chi,s})_i + (W_\chi^s)_i] [(w_{\chi,s})_j + (W_\chi^s)_j] f'_0(\xi_{\chi,s}), \quad \text{where } \mathbf{W}_\chi^s = e(\mathbf{w}_{\chi,s} \cdot \boldsymbol{\Omega}_{\chi,s}) \mathbf{B}. \quad (35)$$

Using the results from Ref. [82], the conductivity for the internode-scattering-induced current is captured by

$$\begin{aligned} \sigma_{ij}^{\text{inter}}(\chi, s) &= \frac{e^2 [\tau_G \rho_{-\chi}^{(0)} - \tau \rho_G^{(0)}] \mathcal{Z}_{\chi,i}^s \zeta_j^\chi}{\rho_G^{(0)} \rho_\chi^{(0)}} + \mathcal{O}(B^3), \\ \rho_\chi^{(0)} &= \sum_{\tilde{s}} \int \frac{d^3 \mathbf{q}}{(2\pi)^3} \{-f'_0(\varepsilon_{\chi,\tilde{s}}(q))\}, \quad \rho_G^{(0)} = \frac{\rho_\chi^{(0)} + \rho_{-\chi}^{(0)}}{2}, \quad \zeta_j^\chi = \sum_{\tilde{s}} \mathcal{Z}_{\chi,j}^{\tilde{s}}, \\ \mathcal{Z}_{\chi,j}^s &= B_j \int \frac{d^3 \mathbf{k}}{(2\pi)^3} \left[e \boldsymbol{\Omega}_{\chi,s}(\mathbf{k}) \cdot \mathbf{v}_{\chi,s}(\mathbf{k}) \{-f'_0(\varepsilon_{\chi,s}(k))\} + (m_{\chi,s}(\mathbf{k}))_j (v_{\chi,s}(\mathbf{k}))_j f''_0(\varepsilon_{\chi,s}(k)) \right], \end{aligned} \quad (36)$$

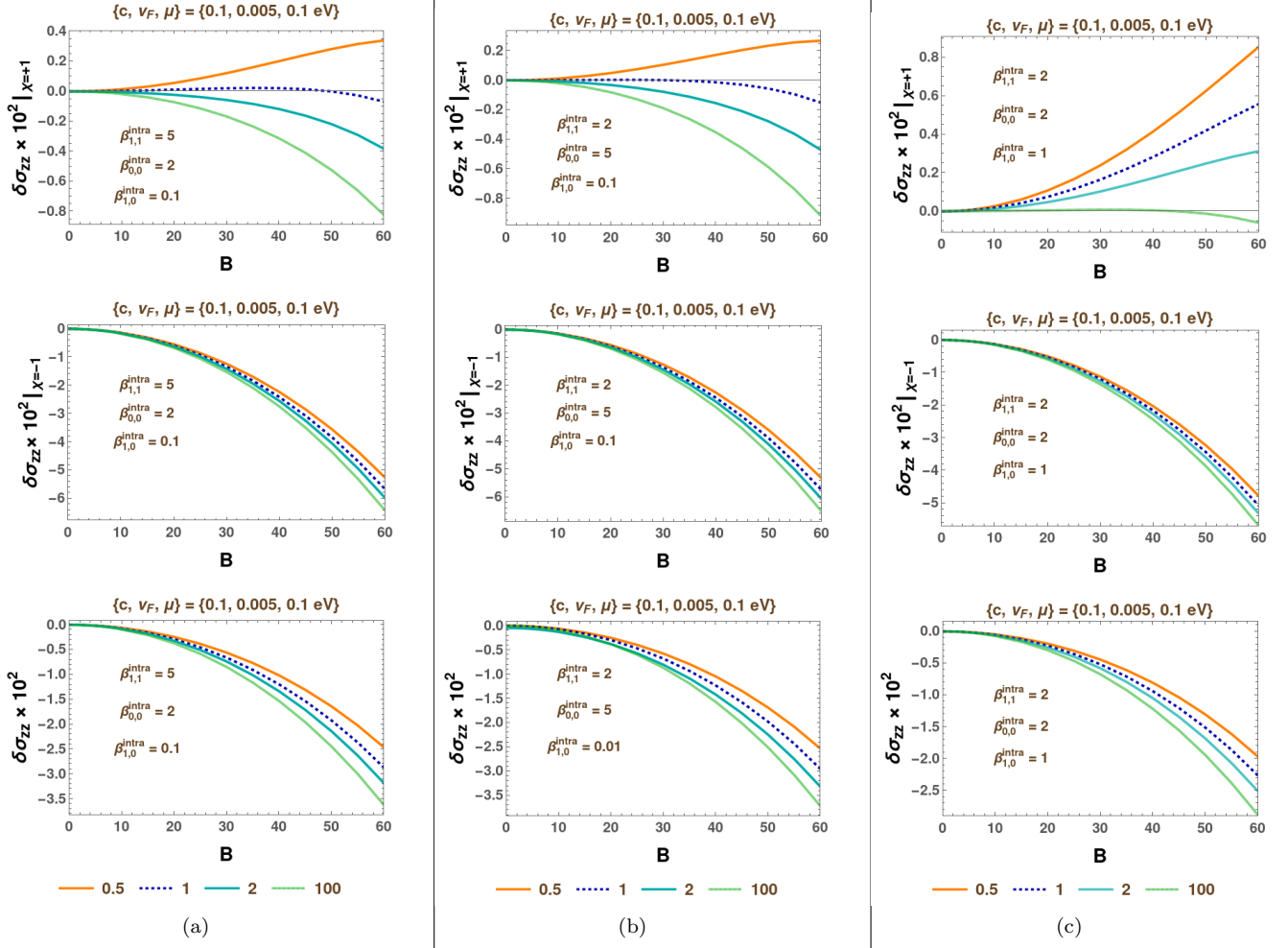


FIG. 5. $\delta\sigma_{zz}$ from the $\{s, \tilde{s}\} = \{0, 0\}$ bands interacting mutually and with the $\{s, \tilde{s}\} = \{1, 1\}$ bands: The curves demonstrate the variation of conductivity of the $\{s, \tilde{s}\} = \{1, 1\}$ bands with B (in eV^2). The top, middle, and bottom panels represent the results for the $\chi = +1$ node, $\chi = -1$ node, and sum over both the nodes, respectively. The plot-legends indicate the values of the ratios $\{\beta_{s,\tilde{s}}^{\text{inter}}/\beta_{s,\tilde{s}}^{\text{intra}}\}$. The three subfigures represent three distinct sets of parameter values, as indicated in the labels.

which is applicable for our isotropic bands. Here, τ_G represents the relaxation time for internode scatterings, which is taken to be the same for all concerned bands. For the special case where we have scatterings between two nodes of the same nature, with no net energy-offset between the nodal points (relative to each other in the BZ), Eq. (36) further simplifies to [82]

$$\sigma_{ij}^{\text{inter}}(\chi, s) = \frac{e^2 \tau}{\rho_1^{(0)}} \left(\frac{\tau_G}{\tau} - 1 \right) \mathcal{Z}_{1,i}^s \sum_{\tilde{s}} \mathcal{Z}_{1,j}^{\tilde{s}}. \quad (37)$$

For the configuration considered here, only the $\sigma_{zz}^{\text{intra}}(\chi, s)$ - and $\sigma_{zz}^{\text{inter}}(\chi, s)$ -components are nonzero. Moreover, due to the isotropic nature of the dispersions, only even powers of B can appear, as also justified by the Onsager-Casimir reciprocity relation, $\sigma_{zz}^{\text{intra(inter)}}(\mathbf{B}) = \sigma_{zz}^{\text{intra(inter)}}(-\mathbf{B})$ [91–93]. Consequently, the answers turn out to be χ -independent.

A. Contribution from intranode parts

For the $s = 1$ and $s = 0$ bands, Eq. (35) evaluates to

$$\begin{aligned} \sigma_{zz}^{\text{dr}}|_{s=1} &= \frac{e^2 \tau \sqrt{4c\mu + v_F} (\sqrt{v_F} - \sqrt{4c\mu + v_F})^2}{(2\pi)^3 \times 6 c^2 \sqrt{v_F}}, & \sigma_{zz}^{\text{bc}}|_{s=1} &= \frac{64 B^2 c^2 e^4 \tau v_F^{3/2} \sqrt{4c\mu + v_F}}{(2\pi)^3 \times 15 (\sqrt{v_F} - \sqrt{4c\mu + v_F})^2}, \\ \sigma_{zz}^{\text{omm}}|_{s=1} &= \frac{-2 B^2 c^2 e^4 \tau v_F^{3/2} \left[12 v_F^2 + 42 c \mu v_F + 16 c \mu \sqrt{v_F (4c\mu + v_F)} + \sqrt{v_F^3 (4c\mu + v_F)} \right]}{(2\pi)^3 \times 15 (4c\mu + v_F)^{3/2} (\sqrt{v_F} - \sqrt{4c\mu + v_F})^2}, \end{aligned} \quad (38)$$

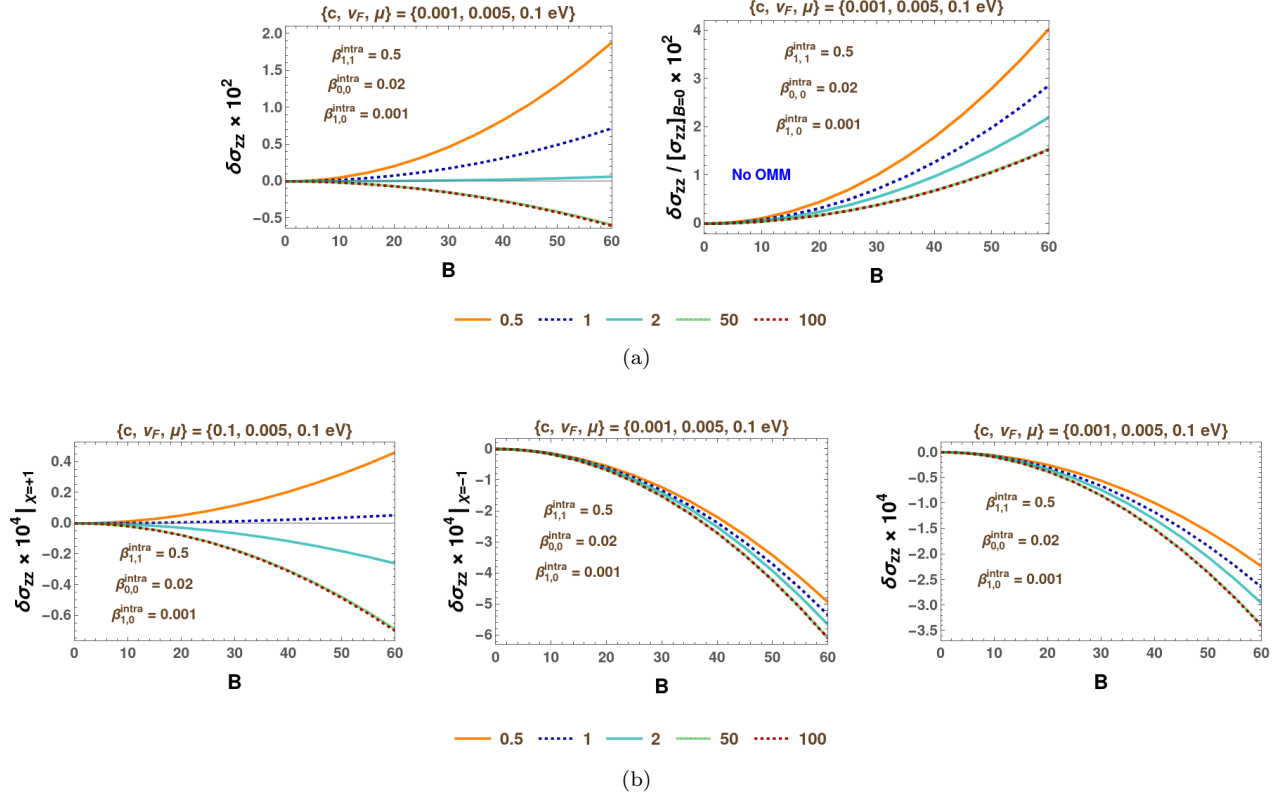


FIG. 6. (a) Net $\delta\sigma_{zz}$ from the for the $\{s, \tilde{s}\} = \{1, 1\}$ bands, when interacting mutually and with the $\{s, \tilde{s}\} = \{0, 0\}$ bands, as B (in eV^2) is cranked up. (b) Node-dependent and net values of $\delta\sigma_{zz}$ for the $\{s, \tilde{s}\} = \{0, 0\}$ bands, as B is varied, when interacting mutually and with the $\{s, \tilde{s}\} = \{1, 1\}$ bands,. The plot-legends indicate the values of the ratios $\{\beta_{s,\tilde{s}}^{\text{inter}}/\beta_{s,\tilde{s}}^{\text{intra}}\}$.

$$\sigma_{zz}^{\text{dr}}|_{s=0} = \frac{4e^2\mu^{3/2}\tau}{(2\pi)^3 \times 3\sqrt{c}v_F}, \quad \sigma_{zz}^{\text{bc}}|_{s=0} = 0, \quad \sigma_{zz}^{\text{omm}}|_{s=0} = \frac{7B^2\sqrt{c}e^4\tau v_F^{5/2}}{(2\pi)^3 \times 30\mu^{3/2}}. \quad (39)$$

Here, the superscripts, “dr”, “bc”, and “omm”, indicate the Drude (i.e., B -independent), BC-only, and OMM-induced contributions, respectively. For $s = 1$, σ_{zz}^{bc} and σ_{zz}^{omm} come with opposite signs. For the parameter regions for μ , v_F , and c considered here, the magnitude of the latter is always smaller than that of the former, with the overall response remaining positive. This is in agreement with the conclusions reached in Ref. [16], where the quadratic-in-momentum corrections were not considered. For the $s = 0$ bands, the B -dependent part is solely sourced by the OMM and the relevant terms involve a product of two terms arising from OMM. Such a product term gives only a positive contribution, as is reflected in $\sigma_{zz}^{\text{omm}}|_{s=0}$. In fact, the negative parts in $\sigma_{zz}^{\text{omm}}|_{s=1}$ have arisen from integrands containing a product of one power of BC-only and one power of OMM-only terms, cancelling out (and overpowering) the OMM-only positive terms. From all these discussions, the conclusion is that, $\sigma_{zz}^{\text{inter}} = \sigma_{zz}^{\text{bc}} + \sigma_{zz}^{\text{omm}}$ turns out to be exclusively positive for all the bands in this relaxation-time approximation, without any possibility of sign-flips.

B. Contribution from internode parts

Evaluating Eq. (37) for our system, we obtain

$$\begin{aligned} \sigma_{zz}^{\text{inter}}|_{s=1} &= \frac{B^2 e^4 \tau (c v_F)^{3/2} \sqrt{4c\mu + v_F} \left(\sqrt{\frac{v_F}{4c\mu + v_F}} + 6 \right) \left[\sqrt{c\mu v_F} \left(\sqrt{\frac{v_F}{4c\mu + v_F}} + 6 \right) + v_F \right]}{36 \pi^2 \sqrt{\mu} \left(-v_F \sqrt{4c\mu + v_F} + 2c\mu \sqrt{v_F} + \sqrt{c\mu v_F} \sqrt{4c\mu + v_F} + v_F^{3/2} \right)} \left(\frac{\tau_G}{\tau} - 1 \right), \\ \sigma_{zz}^{\text{inter}}|_{s=0} &= \frac{B^2 c e^4 \tau v_F^2 \sqrt{4c\mu + v_F}}{36 \pi^2 \mu \left(-v_F \sqrt{4c\mu + v_F} + 2c\mu \sqrt{v_F} + \sqrt{c\mu v_F} \sqrt{4c\mu + v_F} + v_F^{3/2} \right)} \left(\frac{\tau_G}{\tau} - 1 \right). \end{aligned} \quad (40)$$

In realistic systems (see, for example, Ref. [8]), $\tau_G/\tau \gg 1$, leading to $\sigma_{zz}^{\text{inter}}$ being positive for each band, and with a magnitude much much larger than $\sigma_{zz}^{\text{intra}}$.

C. Overall characteristics

The net conductivity from each band turns out to be positive, with the internode part being the dominating contribution. Hence, we find that the relaxation-time approximation is unable to capture the actual characteristics that have been obtained by the exact solutions of the Boltzmann equations. Albeit, the results obtained by the former can be improved upon by introducing interband scatterings within a single node and, perhaps, by introducing band-dependent phenomenological values of the relaxation times.

V. SUMMARY, DISCUSSIONS, AND FUTURE PERSPECTIVES

In this paper, we have addressed the crucial question of determining the nature of longitudinal magnetoconductivity for multifold semimetals, taking the TSM with quadratic-corrections as an example. A TSM's threefold-degenerate nodal points ensure that multiple bands contribute to transport at each node, although this signature was missed/ignored in earlier works [16, 85], because the $s = 0$ band provided zero input due its designation as a flat/nondispersive band. However, the flatness of this band is an artifact of retaining only the linear-in-momentum terms in the effective Hamiltonian in the vicinity of a given node, which is corrected in our approach by including the leading-order corrections $\propto k^2$. Indeed, the $s = 0$ bands harbour nontrivial topological characteristics on the virtue of possessing nonzero values of OMM, although having zero BC (or vanishing Chern numbers). Hence, the ck^2 term in the Hamiltonian [cf. Eq. (1)] enables us to account for the actual responsible that must be observable in contemporary experiments [8]. Our calculations and results also act to bring out the importance of going beyond the relaxation-time approximation, as the full/correct picture is not obtained by confining ourselves to such an approximation. This is explicitly and quantitatively verified by computing and comparing the answers obtained from the two approaches.

In the future, it will be worthwhile to repeat our calculations for a magnetic field which is not exactly collinear with the electric field [84]. This will cause nonzero components of conductivity in the form of Hall and planar-Hall response. Another avenue to explore is to introduce nonzero tilts in the spectra [27, 33, 35, 90, 94]. Since realistic bandstructures indeed show tilting, this constitutes an important aspect. In particular, tilting can cause linear-in- B terms to appear in the conductivity [27, 33, 35, 84, 90, 94], satisfying Onsager-Casimir reciprocity relations. Next, one would like to determine the characteristics of magneto-optical conductivity under quantising magnetic fields [54–56] for the TSMs. A straightforward but interesting complementary direction is to compute transmission characteristics in tunneling problems in the quadratic-corrected TSMs, in the same spirit as done in some of our earlier works [9, 24, 95–98]. A nonlinear-in-momentum dependence in the propagation direction of the quasiparticles bring into the existence of evanescent waves, which render the problem computationally challenging to solve [24, 97–102].

ACKNOWLEDGMENTS

We thank Carsten Timm for useful discussions.

APPENDIX: MATRIX EQUATION FOR DETERMINING THE UNKNOWN COEFFICIENTS

respectively. The various symbols represent the following integrals:

$$\begin{aligned}
c_{\alpha_\chi s}^4 &= \int d\theta \mathcal{F}_{\chi,s}(k, \theta) \cos^4 \theta, \quad s_{\alpha_\chi s}^4 = \int d\theta \mathcal{F}_{\chi,s}(k, \theta) \sin^4 \theta, \quad cs_{\alpha_\chi s}^{22} = \int d\theta \mathcal{F}_{\chi,s}(k, \theta) \cos^2 \theta \sin^2 \theta, \\
hc_{\alpha_\chi s}^2 &= \int d\theta \mathcal{F}_{\chi,s}(k, \theta) \cos^2 \theta h_{\chi,s}(\mu, \theta), \quad hs_{\alpha_\chi s}^2 = \int d\theta \mathcal{F}_{\chi,s}(k, \theta) \sin^2 \theta h_{\chi,s}(\mu, \theta), \\
hc_{\alpha_\chi s}^4 &= \int d\theta \mathcal{F}_{\chi,s}(k, \theta) \cos^4(\theta/2) h_{\chi,s}(\mu, \theta), \quad hs_{\alpha_\chi s}^4 = \int d\theta \mathcal{F}_{\chi,s}(k, \theta) \sin^4(\theta/2) h_{\chi,s}(\mu, \theta), \\
c_{\alpha_\chi s}^8 &= \int d\theta \mathcal{F}_{\chi,s}(k, \theta) \cos^8(\theta/2), \quad s_{\alpha_\chi s}^8 = \int d\theta \mathcal{F}_{\chi,s}(k, \theta) \sin^8(\theta/2), \quad cs_{\alpha_\chi s}^{44} = \int d\theta \mathcal{F}_{\chi,s}(k, \theta) \cos^4(\theta/2) \sin^4(\theta/2), \\
cs_{\alpha_\chi s}^{42} &= \int d\theta \mathcal{F}_{\chi,s}(k, \theta) \cos^4(\theta/2) \sin^2 \theta, \quad ss_{\alpha_\chi s}^{42} = \int d\theta \mathcal{F}_{\chi,s}(k, \theta) \sin^4(\theta/2) \sin^2 \theta,
\end{aligned} \tag{41}$$

where

$$\alpha_\chi = \begin{cases} 1 & \text{for } \chi = +1 \\ 2 & \text{for } \chi = -1 \end{cases}, \tag{42}$$

and

$$\mathcal{F}_{\chi,s}(\mu, \theta) = \tau_{\chi,s}(\mu, \theta) \frac{\sin \theta k^3 \mathcal{D}_{\chi,s}^{-1}(k, \theta)}{|\mathbf{k} \cdot \mathbf{w}_{\chi,s}(\mathbf{k})|} \Big|_{k=k_F^{\chi,s}(\theta)}. \tag{43}$$

-
- [1] A. A. Burkov and L. Balents, Weyl semimetal in a topological insulator multilayer, *Phys. Rev. Lett.* **107**, 127205 (2011).
 - [2] N. P. Armitage, E. J. Mele, and A. Vishwanath, Weyl and Dirac semimetals in three-dimensional solids, *Rev. Mod. Phys.* **90**, 015001 (2018).
 - [3] B. Yan and C. Felser, Topological materials: Weyl semimetals, *Annual Rev. of Condensed Matter Phys.* **8**, 337 (2017).
 - [4] I. Mandal and K. Saha, Thermoelectric response in nodal-point semimetals, *Ann. Phys. (Berlin)* **536**, 2400016 (2024).
 - [5] B. Bradlyn, J. Cano, Z. Wang, M. G. Vergniory, C. Felser, R. J. Cava, and B. A. Bernevig, Beyond Dirac and Weyl fermions: Unconventional quasiparticles in conventional crystals, *Science* **353** (2016).
 - [6] F. Flicker, F. de Juan, B. Bradlyn, T. Morimoto, M. G. Vergniory, and A. G. Grushin, Chiral optical response of multifold fermions, *Phys. Rev. B* **98**, 155145 (2018).
 - [7] I. Mandal and H. Freire, Transport properties in non-Fermi liquid phases of nodal-point semimetals, *Journal of Physics: Condensed Matter* **36**, 443002 (2024).
 - [8] F. Balduini, A. Molinari, L. Rocchino, V. Hasse, C. Felser, M. Sousa, C. Zota, H. Schmid, A. G. Grushin, and B. Gotsmann, Intrinsic negative magnetoresistance from the chiral anomaly of multifold fermions, *Nature Communications* **15**, 6526 (2024).
 - [9] I. Mandal, Transmission in pseudospin-1 and pseudospin-3/2 semimetals with linear dispersion through scalar and vector potential barriers, *Phys. Lett. A* **384**, 126666 (2020).
 - [10] I. C. Fulga and A. Stern, Triple point fermions in a minimal symmorphic model, *Phys. Rev. B* **95**, 241116 (2017).
 - [11] S. Nandy, K. Sengupta, and D. Sen, Transport across junctions of pseudospin-one fermions, *Phys. Rev. B* **100**, 085134 (2019).
 - [12] S. Sekh and I. Mandal, Circular dichroism as a probe for topology in three-dimensional semimetals, *Phys. Rev. B* **105**, 235403 (2022).
 - [13] P. Tang, Q. Zhou, and S.-C. Zhang, Multiple types of topological fermions in transition metal silicides, *Phys. Rev. Lett.* **119**, 206402 (2017).
 - [14] Y. Shen, Y. Jin, Y. Ge, M. Chen, and Z. Zhu, Chiral topological metals with multiple types of quasiparticle fermions and large spin Hall effect in the SrGePt family materials, *Phys. Rev. B* **108**, 035428 (2023).
 - [15] I. Mandal, Nature of Andreev bound states in Josephson junctions of triple-point semimetals, *arXiv e-prints* (2024), [arXiv:2406.15350 \[cond-mat.supr-con\]](https://arxiv.org/abs/2406.15350).
 - [16] F. Haidar and I. Mandal, Reflections of topological properties in the planar-Hall response for semimetals carrying pseudospin-1 quantum numbers, *Annals of Physics* **478**, 170010 (2025).
 - [17] Z. Ni, K. Wang, Y. Zhang, O. Pozo, B. Xu, X. Han, K. Manna, J. Paglione, C. Felser, A. G. Grushin, F. de Juan, E. J. Mele, and L. Wu, Giant topological longitudinal circular photo-galvanic effect in the chiral multifold semimetal CoSi, *Nature Communications* **12**, 154 (2021).
 - [18] L. Liang and Y. Yu, Semimetal with both Rarita-Schwinger-Weyl and Weyl excitations, *Phys. Rev. B* **93**, 045113 (2016).
 - [19] I. Boettcher, Interplay of topology and electron-electron interactions in Rarita-Schwinger-Weyl semimetals, *Phys. Rev. Lett.* **124**, 127602 (2020).
 - [20] J. M. Link, I. Boettcher, and I. F. Herbut, *d*-wave superconductivity and Bogoliubov-Fermi surfaces in Rarita-Schwinger-Weyl semimetals, *Phys. Rev. B* **101**, 184503 (2020).
 - [21] H. Isobe and L. Fu, Quantum critical points of $j = \frac{3}{2}$ Dirac electrons in antiperovskite topological crystalline insulators, *Phys. Rev. B* **93**, 241113 (2016).
 - [22] J.-Z. Ma, Q.-S. Wu, M. Song, S.-N. Zhang, E. Guedes, S. Ekahana, M. Krivenkov, M. Yao, S.-Y. Gao, W.-H. Fan, *et al.*, Observation of a singular Weyl point surrounded by charged nodal walls in ptga, *Nature Communications* **12**, 3994 (2021).

- [23] S. Sekh and I. Mandal, Magnus Hall effect in three-dimensional topological semimetals, *Eur. Phys. J. Plus* **137**, 736 (2022).
- [24] I. Mandal, Transmission and conductance across junctions of isotropic and anisotropic three-dimensional semimetals, *European Physical Journal Plus* **138**, 1039 (2023).
- [25] I. Mandal, Andreev bound states in superconductor-barrier-superconductor junctions of Rarita-Schwinger-Weyl semimetals, *Phys. Lett. A* **503**, 129410 (2024).
- [26] R. Ghosh, F. Haidar, and I. Mandal, Linear response in planar Hall and thermal Hall setups for Rarita-Schwinger-Weyl semimetals, *Phys. Rev. B* **110**, 245113 (2024).
- [27] I. Mandal, S. Saha, and R. Ghosh, Signatures of topology in generic transport measurements for Rarita-Schwinger-Weyl semimetals, *Solid State Communications* **397**, 115799 (2025).
- [28] D. Xiao, M.-C. Chang, and Q. Niu, Berry phase effects on electronic properties, *Rev. Mod. Phys.* **82**, 1959 (2010).
- [29] G. Sundaram and Q. Niu, Wave-packet dynamics in slowly perturbed crystals: Gradient corrections and Berry-phase effects, *Phys. Rev. B* **59**, 14915 (1999).
- [30] A. Graf and F. Piéchon, Berry curvature and quantum metric in N -band systems: An eigenprojector approach, *Phys. Rev. B* **104**, 085114 (2021).
- [31] A. Knoll, C. Timm, and T. Meng, Negative longitudinal magnetoconductance at weak fields in Weyl semimetals, *Phys. Rev. B* **101**, 201402 (2020).
- [32] R. Ghosh and I. Mandal, Electric and thermoelectric response for Weyl and multi-Weyl semimetals in planar Hall configurations including the effects of strain, *Physica E: Low-dimensional Systems and Nanostructures* **159**, 115914 (2024).
- [33] R. Ghosh and I. Mandal, Direction-dependent conductivity in planar Hall set-ups with tilted Weyl/multi-Weyl semimetals, *Journal of Physics: Condensed Matter* **36**, 275501 (2024).
- [34] L. Medel, R. Ghosh, A. Martín-Ruiz, and I. Mandal, Electric, thermal, and thermoelectric magnetoconductivity for Weyl/multi-Weyl semimetals in planar Hall set-ups induced by the combined effects of topology and strain, *Scientific Reports* **14**, 21390 (2024).
- [35] I. Mandal, Anisotropic conductivity for the type-I and type-II phases of Weyl/multi-Weyl semimetals in planar Hall set-ups, *arXiv e-prints* (2024), [arXiv:2410.05028 \[cond-mat.mes-hall\]](#).
- [36] F. D. M. Haldane, Berry curvature on the Fermi surface: Anomalous Hall effect as a topological Fermi-liquid property, *Phys. Rev. Lett.* **93**, 206602 (2004).
- [37] P. Goswami and S. Tewari, Axionic field theory of $(3+1)$ -dimensional Weyl semimetals, *Phys. Rev. B* **88**, 245107 (2013).
- [38] A. A. Burkov, Anomalous Hall effect in Weyl metals, *Phys. Rev. Lett.* **113**, 187202 (2014).
- [39] S.-B. Zhang, H.-Z. Lu, and S.-Q. Shen, Linear magnetoconductivity in an intrinsic topological Weyl semimetal, *New Journal of Phys.* **18**, 053039 (2016).
- [40] Q. Chen and G. A. Fiete, Thermoelectric transport in double-Weyl semimetals, *Phys. Rev. B* **93**, 155125 (2016).
- [41] S. Nandy, G. Sharma, A. Taraphder, and S. Tewari, Chiral anomaly as the origin of the planar Hall effect in Weyl semimetals, *Phys. Rev. Lett.* **119**, 176804 (2017).
- [42] S. Nandy, A. Taraphder, and S. Tewari, Berry phase theory of planar Hall effect in topological insulators, *Scientific Reports* **8**, 14983 (2018).
- [43] K. Das and A. Agarwal, Linear magnetochiral transport in tilted type-I and type-II Weyl semimetals, *Phys. Rev. B* **99**, 085405 (2019).
- [44] I. Mandal, Effects of time-periodic drive in the linear response for planar-Hall set-ups with Weyl and multi-Weyl semimetals, *arXiv e-prints* (2025), [arXiv:2503.14406 \[cond-mat.mes-hall\]](#).
- [45] K. Das and A. Agarwal, Thermal and gravitational chiral anomaly induced magneto-transport in Weyl semimetals, *Phys. Rev. Res.* **2**, 013088 (2020).
- [46] S. Das, K. Das, and A. Agarwal, Nonlinear magnetoconductivity in Weyl and multi-Weyl semimetals in quantizing magnetic field, *Phys. Rev. B* **105**, 235408 (2022).
- [47] O. Pal, B. Dey, and T. K. Ghosh, Berry curvature induced magnetotransport in 3D noncentrosymmetric metals, *Journal of Phys.: Condensed Matter* **34**, 025702 (2022).
- [48] O. Pal, B. Dey, and T. K. Ghosh, Berry curvature induced anisotropic magnetotransport in a quadratic triple-component fermionic system, *Journal of Phys.: Condensed Matter* **34**, 155702 (2022).
- [49] L. X. Fu and C. M. Wang, Thermoelectric transport of multi-Weyl semimetals in the quantum limit, *Phys. Rev. B* **105**, 035201 (2022).
- [50] Y. Araki, Magnetic textures and dynamics in magnetic Weyl semimetals, *Ann. Phys. (Berlin)* **532**, 1900287 (2020).
- [51] Y. P. Mizuta and F. Ishii, Contribution of Berry curvature to thermoelectric effects, *Proceedings of the International Conference on Strongly Correlated Electron Systems (SCES2013)*, *JPS Conf. Proc.* **3**, 017035 (2014).
- [52] L. Li, J. Cao, C. Cui, Z.-M. Yu, and Y. Yao, Planar Hall effect in topological Weyl and nodal-line semimetals, *Phys. Rev. B* **108**, 085120 (2023).
- [53] F. Hussain Rather, M. Jaffar A., and I. Mandal, Direction-dependent linear response for gapped nodal-line semimetals in planar-Hall configurations, *arXiv e-prints* (2025), [arXiv:2503.10712 \[cond-mat.mes-hall\]](#).
- [54] V. Gusynin, S. Sharapov, and J. Carbotte, Magneto-optical conductivity in graphene, *Journal of Phys.: Condensed Matter* **19**, 026222 (2006).
- [55] M. Stålhammar, J. Larana-Aragon, J. Knolle, and E. J. Bergholtz, Magneto-optical conductivity in generic Weyl semimetals, *Phys. Rev. B* **102**, 235134 (2020).
- [56] S. Yadav, S. Sekh, and I. Mandal, Magneto-optical conductivity in the type-I and type-II phases of Weyl/multi-Weyl semimetals, *Physica B: Condensed Matter* **656**, 414765 (2023).
- [57] M. Papaj and L. Fu, Magnus Hall effect, *Phys. Rev. Lett.* **123**, 216802 (2019).
- [58] D. Mandal, K. Das, and A. Agarwal, Magnus Nernst and thermal Hall effect, *Phys. Rev. B* **102**, 205414 (2020).
- [59] I. Mandal, Signatures of two- and three-dimensional semimetals from circular dichroism, *International Journal of Modern Physics B* **38**, 2450216 (2024).

- [60] J. E. Moore, Optical properties of Weyl semimetals, [National Science Rev.](#) **6**, 206 (2018).
- [61] C. Guo, V. S. Asadchy, B. Zhao, and S. Fan, Light control with Weyl semimetals, [eLight](#) **3**, 2 (2023).
- [62] A. Avdoshkin, V. Kozii, and J. E. Moore, Interactions remove the quantization of the chiral photocurrent at Weyl points, [Phys. Rev. Lett.](#) **124**, 196603 (2020).
- [63] I. Mandal, Effect of interactions on the quantization of the chiral photocurrent for double-Weyl semimetals, [Symmetry](#) **12** (2020).
- [64] D. Bercioux, D. F. Urban, H. Grabert, and W. Häusler, Massless Dirac-Weyl fermions in a \mathcal{T}_3 optical lattice, [Phys. Rev. A](#) **80**, 063603 (2009).
- [65] N. Goldman, D. F. Urban, and D. Bercioux, Topological phases for fermionic cold atoms on the Lieb lattice, [Phys. Rev. A](#) **83**, 063601 (2011).
- [66] Y.-Q. Zhu, D.-W. Zhang, H. Yan, D.-Y. Xing, and S.-L. Zhu, Emergent pseudospin-1 Maxwell fermions with a threefold degeneracy in optical lattices, [Phys. Rev. A](#) **96**, 033634 (2017).
- [67] B. Q. Lv, Z.-L. Feng, J.-Z. Zhao, N. F. Q. Yuan, A. Zong, K. F. Luo, R. Yu, Y.-B. Huang, V. N. Strocov, A. Chikina, A. A. Soluyanov, N. Gedik, Y.-G. Shi, T. Qian, and H. Ding, Observation of multiple types of topological fermions in PdBiSe, [Phys. Rev. B](#) **99**, 241104 (2019).
- [68] Z. Zhu, G. W. Winkler, Q. Wu, J. Li, and A. A. Soluyanov, Triple point topological metals, [Phys. Rev. X](#) **6**, 031003 (2016).
- [69] H. Weng, C. Fang, Z. Fang, and X. Dai, Topological semimetals with triply degenerate nodal points in θ -phase tantalum nitride, [Phys. Rev. B](#) **93**, 241202 (2016).
- [70] P. Tang, Q. Zhou, and S.-C. Zhang, Multiple types of topological fermions in transition metal silicides, [Phys. Rev. Lett.](#) **119**, 206402 (2017).
- [71] H. Weng, C. Fang, Z. Fang, and X. Dai, Coexistence of Weyl fermion and massless triply degenerate nodal points, [Phys. Rev. B](#) **94**, 165201 (2016).
- [72] R. Shen, L. B. Shao, B. Wang, and D. Y. Xing, Single Dirac cone with a flat band touching on line-centered-square optical lattices, [Phys. Rev. B](#) **81**, 041410 (2010).
- [73] Z. Lan, N. Goldman, A. Bermudez, W. Lu, and P. Öhberg, Dirac-Weyl fermions with arbitrary spin in two-dimensional optical superlattices, [Phys. Rev. B](#) **84**, 165115 (2011).
- [74] D. F. Urban, D. Bercioux, M. Wimmer, and W. Häusler, Barrier transmission of Dirac-like pseudospin-one particles, [Phys. Rev. B](#) **84**, 115136 (2011).
- [75] P. He, X. Shen, D.-W. Zhang, and S.-L. Zhu, Simulating the Klein tunneling of pseudospin-one Maxwell particles with trapped ions, [Physics Letters A](#) **383**, 2462 (2019).
- [76] H.-Y. Xu and Y.-C. Lai, Revival resonant scattering, perfect caustics, and isotropic transport of pseudospin-1 particles, [Phys. Rev. B](#) **94**, 165405 (2016).
- [77] S. Nandy, S. Manna, D. Călugăru, and B. Roy, Generalized triple-component fermions: Lattice model, Fermi arcs, and anomalous transport, [Phys. Rev. B](#) **100**, 235201 (2019).
- [78] J. Cayssol and J. N. Fuchs, Topological and geometrical aspects of band theory, [Journal of Physics: Materials](#) **4**, 034007 (2021).
- [79] M. M. H. Polash, S. Yalameha, H. Zhou, K. Ahadi, Z. Nourbakhsh, and D. Vashae, Topological quantum matter to topological phase conversion: Fundamentals, materials, physical systems for phase conversions, and device applications, [Materials Science and Engineering: R: Reports](#) **145**, 100620 (2021).
- [80] H. Nielsen and M. Ninomiya, A no-go theorem for regularizing chiral fermions, [Phys. Lett. B](#) **105**, 219 (1981).
- [81] L. Medel Onofre and A. Martín-Ruiz, Planar Hall effect in Weyl semimetals induced by pseudoelectromagnetic fields, [Phys. Rev. B](#) **108**, 155132 (2023).
- [82] I. Mandal, Chiral anomaly and internode scatterings in multifold semimetals, [Phys. Rev. B](#) **111**, 165116 (2025).
- [83] G. Sharma, S. Nandy, K. V. Raman, and S. Tewari, Decoupling intranode and internode scattering in Weyl fermions, [Phys. Rev. B](#) **107**, 115161 (2023).
- [84] A. Ahmad, K. V. Raman, S. Tewari, and G. Sharma, Longitudinal magnetoconductance and the planar Hall conductance in inhomogeneous Weyl semimetals, [Phys. Rev. B](#) **107**, 144206 (2023).
- [85] A. Ahmad and G. Sharma, Chiral anomaly and longitudinal magnetoconductance in pseudospin-1 fermions, [arXiv e-prints](#) (2024), [arXiv:2412.10500 \[cond-mat.mes-hall\]](#).
- [86] N. Ashcroft and N. Mermin, [Solid State Physics](#) (Cengage Learning, 2011).
- [87] L. Li, J. Cao, C. Cui, Z.-M. Yu, and Y. Yao, Planar hall effect in topological Weyl and nodal-line semimetals, [Phys. Rev. B](#) **108**, 085120 (2023).
- [88] D. Xiao, W. Yao, and Q. Niu, Valley-contrasting physics in graphene: Magnetic moment and topological transport, [Phys. Rev. Lett.](#) **99**, 236809 (2007).
- [89] I. Mandal and K. Saha, Thermopower in an anisotropic two-dimensional Weyl semimetal, [Phys. Rev. B](#) **101**, 045101 (2020).
- [90] I. Mandal, Linear response of tilted anisotropic two-dimensional Dirac cones, [arXiv e-prints](#) (2024), [arXiv:2412.13978 \[cond-mat.mes-hall\]](#).
- [91] L. Onsager, Reciprocal Relations in Irreversible Processes. I., [Phys. Rev.](#) **37**, 405 (1931).
- [92] H. B. G. Casimir, On Onsager's principle of microscopic reversibility, [Rev. Mod. Phys.](#) **17**, 343 (1945).
- [93] P. Jacquod, R. S. Whitney, J. Meair, and M. Büttiker, Onsager relations in coupled electric, thermoelectric, and spin transport: The tenfold way, [Phys. Rev. B](#) **86**, 155118 (2012).
- [94] K. Das and A. Agarwal, Berry curvature induced thermopower in type-I and type-II Weyl semimetals, [Phys. Rev. B](#) **100**, 085406 (2019).
- [95] A. Fang, Z. Q. Zhang, S. G. Louie, and C. T. Chan, Klein tunneling and supercollimation of pseudospin-1 electromagnetic waves, [Phys. Rev. B](#) **93**, 035422 (2016).
- [96] R. Zhu and P. M. Hui, Shot noise and Fano factor in tunneling in three-band pseudospin-1 Dirac-Weyl systems, [Physics Letters A](#) **381**, 1971 (2017).

- [97] Y.-H. Deng, H.-F. Lü, S.-S. Ke, Y. Guo, and H.-W. Zhang, Quantum tunneling through a rectangular barrier in multi-Weyl semimetals, [Phys. Rev. B](#) **101**, 085410 (2020).
- [98] I. Mandal and A. Sen, Tunneling of multi-Weyl semimetals through a potential barrier under the influence of magnetic fields, [Physics Letters A](#) **399**, 127293 (2021).
- [99] S. Banerjee, R. R. P. Singh, V. Pardo, and W. E. Pickett, Tight-binding modeling and low-energy behavior of the semi-Dirac point, [Phys. Rev. Lett.](#) **103**, 016402 (2009).
- [100] I. Mandal, Andreev bound states in Josephson junctions of semi-Dirac semimetals, [Physica B: Condensed Matter](#) **683**, 415918 (2024).
- [101] I. Mandal, Transmission through rectangular potentials in semimetals featuring quadratic dispersion, [Annals of Physics](#) **479**, 170053 (2025).
- [102] I. Mandal, Delta-function-potential junctions with quasiparticles occupying tilted bands with quadratic-in-momentum dispersion, [Current Applied Physics](#) **76**, 26 (2025).